EPICARDIAL TRANSPLANTATION OF ATRIAL APPENDAGE MICROGRAFT PATCH SALVAGES MYOCARDIUM AFTER INFARCTION

Xie Yanbo , Milla Lampinen , Juuso Takala , Vilbert Sikorski , Rabah Soliymani , Miikka Tarkia , Maciej Lalowski , Eero Mervaala , Markku Kupari , Zhe Zheng , Shengshou Hu , Ari Harjula , Esko Kankuri , on behalf of the AADC consortium

PII: S1053-2498(20)31484-4
DOI: https://doi.org/10.1016/j.healun.2020.03.023
Reference: HEALUN 7133

To appear in: *Journal of Heart and Lung Transplantation*

Please cite this article as: Xie Yanbo , Milla Lampinen , Juuso Takala , Vilbert Sikorski , Rabah Soliymani , Miikka Tarkia , Maciej Lalowski , Eero Mervaala , Markku Kupari , Zhe Zheng , Shengshou Hu , Ari Harjula , Esko Kankuri , on behalf of the AADC consortium, EPICARDIAL TRANSPLANTATION OF ATRIAL APPENDAGE MICROGRAFT PATCH SALVAGES MYOCARDIUM AFTER INFARCTION, *Journal of Heart and Lung Transplantation* (2020), doi: https://doi.org/10.1016/j.healun.2020.03.023

EPICARDIAL TRANSPLANTATION OF ATRIAL APPENDAGE MICROGRAFT PATCH SALVAGES MYOCARDIUM AFTER INFARCTION

Xie Yanbo [1*], Milla Lampinen[2*], Juuso Takala[2*], Vilbert Sikorski[2*], Rabah Soliymani[3,4], Miikka Tarkia[2], Maciej Lalowski[3,4], Eero Mervaala[2], Markku Kupari[5], Zhe Zheng[1], Shengshou Hu[1], Ari Harjula[5], Esko Kankuri[2,†] on behalf of the AADC consortium

* Equal contribution

† Corresponding author

[1] FuWai Hospital, Beijing, China

[2] Faculty of Medicine, Department of Pharmacology, University of Helsinki, Finland

[3] Faculty of Medicine, Biochemistry/Developmental Biology, University of Helsinki, Finland

[4] Helsinki Institute of Life Science (HiLIFE), University of Helsinki, Finland

[5] Heart and Lung Center, Helsinki Central Hospital and University of Helsinki, Finland

Address correspondence to: Esko Kankuri MD PhD, Faculty of Medicine, Department of Pharmacology, PO Box 63 (Haartmaninkatu 8), FIN-00014 University of Helsinki, Finland. Email esko.kankuri@helsinki.fi, tel. +358-29-41-25336, fax. +358-2941-25364

Abstract

BACKGROUND: Ischemic heart disease remains the leading cause of mortality and morbidity worldwide despite improved possibilities in medical care. Alongside interventional therapies, such as coronary artery bypass grafting, adjuvant tissue-engineered and cell-based treatments can provide regenerative improvement. Unfortunately, most of these advanced approaches require multiple lengthy and costly preparation stages without delivering significant clinical benefits.

METHODS: We evaluated the effect of epicardially delivered minute pieces of atrial appendage tissue material, defined as atrial appendage micrografts (AAMs), in mouse myocardial infarction model. An extracellular matrix patch was used to cover and fix the AAMs onto the surface of the infarcted heart.

RESULTS: The matrix-covered AAMs salvaged the heart from infarction-induced loss of functional myocardium and attenuated scarring. Site-selective proteomics of injured ischemic and uninjured distal myocardium from AAMs-treated and untreated tissue sections revealed an increased expression of several cardiac regeneration-associated proteins (i.e. periostin, transglutaminases and glutathione peroxidases) as well as activation of pathways responsible for angio- and cardiogenesis in relation to AAMs therapy.

CONCLUSIONS: Epicardial delivery of AAMs encased in an extracellular matrix patch scaffold salvages functional cardiac tissue from ischemic injury and restricts fibrosis after myocardial infarction. Our results support the use of AAMs as tissue-based therapy adjuvants for salvaging the ischemic myocardium.

Introduction

Ischemic heart disease has persistently maintained its rank as the global leading cause of mortality.[1] Replacement of functional myocardium with a non-contractile fibrotic scar after irreversible ischemic injury over-activates compensatory mechanisms, contributes to myocardial rigidity and eventually to the development of heart failure (HF) over time.[2] Therapeutic interventions alleviate symptoms, but fail to restore lost myocardial tissue.[3,4] Regenerative tissue-engineering and cell-based therapies have been suggested to directly or indirectly instigate recovery of tissue function. Many cell-based therapies have poor clinical translatability due to high complexity, costs, lengthy preparation times, requirements for special production facilities, and sometimes frank incompatibility with clinical practice.[5,6] Although a plethora of cell types have been evaluated in clinical trials, none are used as a part of clinical practice.[7]

Studies conducted with cardiac progenitor cells stimulated further interest in functional heart regeneration.[8,9] Unfortunately, some studies were associated with major controversies and the cardiac cell therapy community entered a state of disbelief. The autologous cardiac origin and the claim for a rich cardiac progenitor pool in atrial tissue[10,11,12] support its use for cardiac therapy.[13] The AADC consortium recently demonstrated clinical feasibility of intraoperative processing and epicardial transplantation of autologous atrial appendage micrografts (AAMs).[14,15]

In this study we investigated the functional efficacy and molecular therapeutic mechanisms of epicardial AAMs patch transplantation in a murine model of myocardial infarction (MI) and HF (Figure 1).

Results

Myocardial function

Left ventricular ejection fraction (LVEF) and area under the curve (AUC) analyses spanning the 8-week follow-up period are presented in Figure 2A. Echocardiographic (ECHO) recordings demonstrated improved functional recovery in the AAMs patch group than in the ECM patch and MI groups. Lower initial LVEF values in the Sham group were due to lower weight of the group's mice at the beginning of the experiment.

In all intervention groups, LVEF decline was evident during the first two weeks of the follow-up. The acute declines in LVEF at one-week time-point postoperatively in AAMs patch, ECM patch and MI groups were 18.03 (54.49±2.93%-36.69±2.56%), 19.77 (52.15±3.10%-32.38±2.96%) and 34.94 percent points (58.72±2.58%-23.78±3.16%), respectively, with a significant difference between AAMs patch and MI groups. In the later phase of the follow-up, the LVEF curves of the AAMs and ECM patch groups separated, suggesting prolonged therapeutic effect from the AAMs. Significantly higher mean LVEF values were observed in the AAMs group than in the MI group from 4th week onward until the 7th week of follow-up. The Supplementary Table S1 provides the values of all ECHO parameters.

Figure 2A shows the LVEF measurements and AUC analysis over the entire follow-up period. Only the AAMs patch group demonstrated highly preserved LVEF function compared to MI group. The average LVEF AUC-values were 334.2±26.68 (AAMs patch), 277.1±19.85 (ECM patch), 213.4±28.55 (MI), and 354±8.21 (Sham).

The functional state of the left ventricle was further assessed by strain analyses. AUC data is presented in Figure 2B-E and the complete strain analyses data is available as online supplements (Figure S1 and Table S1). Overall, strain parameters in both patch groups were well preserved, with the greatest preservation in the AAMs patch group.

Mean circumferential strain values (Figure 2B) at the 8-week time-point were -13.5±2.48 (AAMs patch), -12.2±2.87 (ECM patch), -7.0±2.04 (MI) and -15.1±2.57 (Sham). AUC analysis (Figure 2B) revealed preserved function only in the AAMs patch group. The average AUC-values

for circumferential strain were 78.6±15.04 (AAMs patch), 49.9±9.50 (ECM patch), 32.6±11.27 (MI), and 89.46±12.30 (Sham). Mean circumferential strain rates at the end of the follow-up were -4.2±0.65 (AAMs patch), -3.5±0.90 (ECM patch), -2.3±0.45 (MI) and -4.5±0.55 (Sham) and the corresponding AUC-values for the circumferential strain rate were as follows: 11.7±1.98 (AAMs patch), 7.9±1.27 (ECM patch), 5.9±1.56 (MI), and 13.31±1.88 (Sham). Again, the AAMs patch group demonstrated better recovery.

Longitudinal strain showed no decline in either patch group, and only the MI group against the Sham group showed significant decrease (Figure 2D). Longitudinal strain values at the 8-week time-point were -13.4±2.16 (AAMs patch), -16.6±2.83 (ECM patch), -12.9±4.05 (MI) and -14.4±2.41 (Sham) with the corresponding AUC-values being 81.8±22.23 (AAMs patch), 69.1±10.87 (ECM patch), 56.1±15.65 (MI), and 109.4±12.67 (Sham) (Figure 2E). Longitudinal strain rate values at the 8-week time-point were -5.0±0.63 (AAMs patch), -5.2±0.86 (ECM patch), -4.2±0.97 (MI), and -4.8±0.40 (Sham) with the corresponding AUC-values being 31.3±6.88 (AAMs patch), 21.2±2.67 (ECM patch), 17.2±6.00 (MI), and 33.8±5.12 (Sham).

Atrial natriuretic peptide (ANP) expression

ANP mRNA expression (Figure 2F) was significantly lesser in both patch groups (3.6±1.24 for AAMs, and 2.3±0.41 for ECM) compared to expression in the MI group (7.9±1.70). The possible presence of ANP-expressing AAMs may raise ANP values in the AAMs patch group.

Fibrosis

Build-up of fibrous tissue was analyzed by the scar transmurality index (scar thickness divided by the wall thickness at measurement point, Figure 3A) and ventricular wall thickness (Figure 3B). The mean scar transmurality index values were 50.2±3.69% (AAMs patch), 53.1±3.54% (ECM patch), and 81.3±4.26% (MI) with the least fibrosis in the AAMs patch group. The mean ventricular wall thicknesses were 0.21±0.01 cm (AAMs patch), 0.16±0.08 cm (ECM patch), 0,061±0.071 cm (MI), and 0.15±0.094 cm (Sham). The greater thickness in the AAMs patch group can be attributable to the transplanted micrografts. The AAMs group also had the lowest degree of scar dispersion by planimetry (Figure 3C), although both patch groups were significantly different from the MI group. The mean scar dispersions were 51.4±13.7° (AAMs

patch), 59.4±14.1° (ECM patch), and 152.4±9.0° (MI). Moreover, the spread of epicardial patch was 135.3±4.7° in the AAMs patch and 161.7±12.8° in the ECM patch group. Figure 3D shows representative histological images from each group.

Endocardial interstitial fibrosis

Overall, the degree of tissue fibrosis in endocardial myocardium was lower in both patch groups than in the MI group. The endocardial area is the least tolerant to hypoxia and is the first region to be damaged and scarred after an ischemic insult. Evaluation of the endocardial fibrosis, with collagen subtype characterization, is presented in Figure 4. In all analyses, both patch groups demonstrated significantly lesser fibrosis compared to the MI group. The mean content of collagen fibers was 3.23±0.83% (AAMs patch), 1.67±0.55% (ECM patch), and 15.2±1.96% (MI); bright fibers 0.035±0.013% (AAMs patch), 0.005±0.002% (ECM patch), and 0.309±0.088% (MI); green fibers 0.77±0.19% (AAMs patch), 0.28±0.062% (ECM patch), and 4.54±0.65% (MI); orange fibers 2.43±0.65% (AAMs patch), 1.38±0.53% (ECM patch), and 10.32±1.32% (MI).

Myocardium immunohistochemistry

We evaluated the preservation of myocardial tissue with anti-cardiac troponin T (cTnT) immunohistochemistry (Figure 5A-B) and by quantifying the Picrosirius Red-negative area (Figure 5C-D). The area of cTnT-positive tissue in the subtransplant area was larger in both patch groups than in the MI group. However, some MI-induced damage was observable across all interventional groups against Sham group. cTnT-positive tissue in the subtransplant encompassed 49.4±1.94% (AAMs patch), 53.6±2.46% (ECM patch), 35.0±2.28% (MI), and 99.68±3.52% (Sham). Within the site of infarction, significantly more Picrosirius Red-negative nodules were found in the AAMs patch group than in the ECM patch or MI groups (Figure 5C). Non-collagenous nodule amounts were 3.6±0.71 (AAMs patch), 0.7±0.28 (ECM patch) and 1.1±0.24 (MI). The nodules observed in the AAMs patch group were also significantly the largest as compared to other groups (Figure 5C). The mean Picrosirius Red-negative tissue area encompassed 1205±258 pixels (AAMs patch), 141±49 pixels (ECM patch), and 258±75 pixels (MI) (see Figure 5D). These nodules remained cTnT negative (Figure 5B), suggesting that they do not represent contractile cardiac tissue. Figure 5E presents representative histological sections from each study group stained against cTnT.

Proteomics

In a separate experiment designed to compare AAMs and ECM patch molecular tissue-level responses with the same MI model and the 8-week follow-up, label-free site-targeted proteomics was performed on samples from the following areas: (1) ECM or AAMs patch (transplant), (2) subtransplant and (3) distal septal myocardium (Figure 1). Our aim was to specifically dissect the therapeutic effect of AAMs from that of the ECM patch. All quantified and differentially expressed proteins (DEPs) are presented in Data File S1 and the proteomics data have been uploaded to the Mass Spectrometry Interactive Virtual Environment (MassIVE) for in-depth review (Supplemental data). The quantified proteins (1,005 in total) were assessed utilizing a Spearman correlation heatmap, which confirmed site-specific dissection of the transplant, subtransplant and remote septal samples. Samples from the patch transplant area clustered as a separate group, while the myocardial samples from the subtransplant and septal areas formed another major cluster. Within this myocardial cluster, samples from the AAMs patch-treated group from both subtransplant and septal areas clustered separately from ECM patch samples without micrograft therapy, suggesting a widespread independent therapeutic effect of AAMs (Figure S2). By comparing the AAMs patch group to the ECM patch controls, we identified 293 DEPs (45 upregulated and 248 downregulated) in the transplant area. In the subtransplant area, 216 DEPs were characterized (151 upregulated and 65 downregulated), while in the septal area, 43 DEPs were identified (42 upregulated and 1 downregulated). All DEPs were scrutinized using Ingenuity® Pathway Analysis (IPA®) software to reveal associated canonical pathways, biological functions and disease states.

Transplant/patch zone—DEPs associated with the pathways for *Oxidative phosphorylation* (activation), *Actin cytoskeleton signaling* (activation), *Sirtuin and calcium signaling* (inactivation) were altered in the transplant zone of micrograft-treated vs non-treated tissue (Figure 6A). In transplant, the diseases and functions feature revealed processes related to the survival of cells and tissues. Specifically, functional categories including *Cell death* and *Necrosis* were significantly downregulated (B-H z-scores -2.99 and -3.43, respectively; Figure 6B), while those related to *Cell survival* and *Cell viability* were upregulated (+3.09 and +3.36, respectively; Figure 6B).

Subtransplant zone—Pathways related to cytoskeletal changes and reorganization were activated in the AAMs patch-treated subtransplant zone: *Regulation of actin-based motility by Rho, RhoA signaling* and *Actin cytoskeleton signaling* (Figure 6A). From a metabolic perspective, *Oxidative phosphorylation* was significantly decreased, whereas *Glutathione redox reactions I* were significantly altered with increased expression of enzymes GPX3, GPX1, and GSTM2 in the AAMs patch-treated group (Figure 6A and Data File S1). Notably, functions related to muscle cell, especially cardiomyocyte, viability and new muscle formation (*Formation of musc*le [B-H z-score +2.80], *Differentiation of muscle* and *muscle cells* [+1.90], *Apoptosis* and *cell death of muscle cells* [-1.91, -1.92, respectively]) were significantly activated (Figure 6B). The inflammatory response (*Inflammation of organ* [-2.367]) and *Oxidative stress* (-2.236) showed decreased activity in the AAMs patch-treated group compared the ECM patch group (Figure 6B). Interestingly, we found a 1.518-fold increase in expression level of matricellular protein periostin (POSTN) and 1.663-fold overexpression of tissue transglutaminase-2 enzyme (TGM2) with AAMs transplantation (Figure 7 and Data File S1). These protein-level changes provide molecular-level insight into the AAMs' therapeutic mechanism of action.

Septal zone—Similar to the subtransplant area, *Actin cytoskeleton signaling* and *RhoA signaling* pathways were predicted to be activated by the AAMs. *Glutathione redox reactions I*, with increased expression levels of GPX3 and GSTM2 enzymes, were also significantly altered (Figure 6A, Data File S1). In the AAMs patch group, functions related to a dominant prosurvival effect in remote septum were increased. At the cellular level, *Cell viability* was predicted to be activated (z-score +2.546), while *Cell death* and *Apoptosis* were decreased (z-scores -2.241 and -2.685, respectively, Figure 6B). At the system level, the functions *Morbidity or mortality* and *Organismal death* were predicted to be decreased (z-scores -2.481 and -2.793, respectively, Figure 6B). Notably, overexpression of both matricellular protein POSTN (1.852-fold) and TGM2 enzyme (1.996-fold) were also detected here following AAMs transplantation suggesting a wide-spread therapeutic effect (Figure 7).

All associated canonical pathways as well as biological functions and disease states are presented in Figures S3 and S4. Supplemental Table S2 further presents all associated DEPs to each canonical pathway, biological function and disease state.

Immunohistochemistry and qRT-PCR

To qualitatively assess the expression of selected DEPs identified, we performed immunohistochemical staining for POSTN, TGM2 and GPX1 (see Figure 8A). POSTN expression localized specifically to the extracellular space of the scar-myocardium interphase mostly in the subtransplant area. This kind of spatial staining pattern is well in line with the earlier reports on POSTN expression in the heart after acute MI.[16] On the other hand, TGM2 expression mainly localized to the patch and intracellular compartment of the cardiomyocytes near the minor scar areas while GPX1 expression demonstrated less pronounced staining but localized in the myocardium to the cardiomyocytes near the scar areas and vascular walls and more intense in the patch areas. Results from quantitative real-time PCR (qRT-PCR) confirmed overexpression, in both subtransplant and septal zones, for *Postn*, *Myh7* and *Gpx3* (Figure 8B). The mRNA expression levels for *Postn*, *Myh7* and *Gpx3* were significantly higher only in AAMs patch group when compared to the Sham (P=0.010, P=0.014 and P=0.028 respectively). Moreover, the expression of *Gpx3* was higher in AAMs patch compared to ECM patch group (P=0.046). *Tgm2* mRNA levels did not show significant changes between groups. When comparing the gene and protein expression results, it is important to consider the substantial differences and variation in biological regulation and temporal dynamics between transcription and translation.[17]

Discussion

In a murine model of MI and HF, epicardial patch therapy demonstrated significantly improved cardiac function, greatly preserved myocardial structure, attenuated ventricular wall scarring, and dramatically restricted tissue damage. Myocardial site-targeted proteomics revealed the selective cell and molecular-level therapeutic effects of AAMs. These included activation of cardiomyogenesis, angiogenesis and anti-inflammation pathways, as well as reduction of oxidative stress.

Cell-based therapies have long been investigated for their ability to deliver regenerative effects. Atrial appendages act as niches for cardiac progenitor cells and serve as a rational autologous source of myocardial tissue for therapy due to their easy accessibility and relative redundancy for cardiac function.[11,12] We mechanically disaggregate the atrial appendage tissue after harvesting to yield micrografts ready for epicardial transplantation.[18]

Here, we utilized mass-spectrometry-based quantitative proteomics to decipher myocardial site-specific responses to epicardial AAMs after MI. We demonstrate a widespread cardioprotective effect reaching from the subtransplant myocardium to remote myocardial areas. In the subtransplant area, decreased oxidative metabolism and oxidative stress with increased glutathione metabolism suggest an AAMs-induced change in metabolism towards glycolysis, a process associated with improved regeneration capacity in multiple studies.[19-23] We propose that AAMs induced, likely through a paracrine mechanism, a metabolic shift from oxidative to glycolytic metabolism in the ischemically challenged subtransplant area and a pro-reparative microenvironment for surviving cardiomyocytes, ultimately setting the stage for functional recovery. This effect is further supported by our observation that functions such as “Formation of muscle” and “Differentiation of muscle cells” were activated. Moreover, restoration of functional myocardial tissue is not merely a process of cardiomyocytes, but necessitates formation of new ECM, blood vessels, and lymphatics, all processes of which are mostly orchestrated by cell types other than cardiomyocytes. Our findings demonstrate increased angiogenesis, vasculogenesis, and

widespread prosurvival changes in the myocardium, which indicate induction of a protective and restorative myocardial environment by AAMs.

Increased expression of the cardiomyocyte mitogen and matricellular protein POSTN in both the subtransplant and remote septal zones, further clarifies the cellular and molecular mechanisms of AAMs patch transplantation. The secreted matricellular protein POSTN mediates cell-matrix interactions and repair after tissue injury.[24,25] Our data support the association of POSTN expression and myocardial regenerative signaling via the Rho-kinase pathway.[16] During tissue repair and healing after myocardial infarction, POSTN is secreted to the cardiac interstitium by activated cardiac fibroblasts[16] POSTN to stimulate cardiomyocyte cell cycle re-entry and prevent myocardial rupture after infarction.[16,24]

In the subtransplant myocardium, AAMs selectively increased expression of proteins associated with muscle formation, vasculature development, and glutathione metabolism. DEPs were also negatively associated with cellular infiltration. In both subtransplant and septal myocardium, remote to the transplant site, we discovered increased expression of proteins associated with cardiomyocyte contraction (including MYH7, MYL1, MYL6, MYL12B, ACTA1, ACTN4, DES and CAMK2D). Interestingly, the expression of proteins involved in glutathione metabolism and antioxidant defenses (GSTM2, GSTA4, GPX3) were also significantly increased in the subtransplant and remote septal sites treated by AAMs patch therapy compared with those treated by ECM patch therapy without micrografts. The observed *Gpx3* gene expression difference between AAMs and ECM patch groups further strengthens this association of the AAMs mechanism of action via enhanced myocardial antioxidant defenses. In addition, we found a significant increase in cell viability and a significant decrease in cell death and apoptosis in the septal zone in AAMs patch-treated hearts. This prosurvival action is a documented paracrine effect of cardiac stem/progenitor cell therapy.[26]

Interestingly, the AAMs treatment suppressed inflammatory reactions in the ischemia-challenged subtransplant zone and increased angiogenesis. Proteins associated with muscle cell differentiation were also upregulated in this zone treated with AAMs. Thus, our results suggest that

AAMs can modulate the inflammatory response following MI in a way that promotes functional myocardial recovery.

While the AAMs selectively induce therapeutic myocardial signaling and protein expression after MI, our results indicate that the ECM patch itself also protects against experimental MI and fibrosis. As a mechanically supportive structure, the epicardial ECM patch can alter the biomechanics of the failing left ventricle in a beneficial manner. By increasing wall thickness, ECM patch transplantation can relieve tension in the myocardial wall and subsequently reduce oxygen demand. An epicardial ECM patch may also modify the mechanical force vectors along the ventricular wall to favor an energetically more beneficial contraction.

Although our study provided indirect insights into AAMs survival on the epicardial surface after MI, a targeted evaluation of the extent of autologous graft survival utilizing AAMs-specific experimental long-term labeling methodologies would be required to unequivocally address the extent and duration of a graft survival. Interestingly, however, we found an abundant tissue nodules staining, negative for collagen using Picrosirius Red. The higher expression of ANP mRNA that was observed in AAMs patch group's transplant zone and apices relative to same areas in the ECM patch group, can also indicate persistence of the AAMs.

This study complements our previously reported first clinical application of autologous AAMs patch epicardial transplantation,[14] and the clinical open label safety and feasibility trial (ClinicalTrials.gov identifier NCT02672163).[15] Our results here provide insights into the mechanisms of action of epicardial AAMs patch transplantation, and associate its therapeutic effects, reduced cardiac fibrosis and preservation of functional myocardium, with activation of pathways responsible for angio- and cardiogenesis in the ischemically damaged myocardium. Contrary to the long-lasting trend of developing cardiac cellular therapies with increasing complexity, our results underscore the therapeutic possibilities of readily clinically applicable and straight-forward autologous procedures.

In conclusion, the therapeutic effect of the AAMs patch is mediated through multifaceted synergy between 1) mechanical support with ventricular unloading by the ECM patch transplantation, as demonstrated by improved ECHO parameters, attenuated fibrosis and

preservation of troponin T-positive myocardium in both acellular ECM as well as in AAMs patch-treated groups; 2) enhanced cardiomyocyte contractility through expression of proteins associated with contractile apparatus and Ca2+ signaling in the AAMs patch group; 3) enhanced reparative microenvironment through activated anaerobic glycolysis, angiogenesis and cell viability; 4) decreased oxidative stress and enhanced antioxidant protection by increased glutathione metabolism; 5) upregulated CM mitogenic matricellular POSTN; and 6) modulated inflammation. These results provide a molecular basis for epicardial AAMs patch transplantation therapy in ischemic heart failure for myocardial rescue and repair.

Methods

A full-length description of the methods is available as an online-only data supplement (Detailed Materials and Methods). Figure 1 summarizes the study protocol. A brief overview of the methods is presented here.

Both atrial appendages were harvested and processed to AAMs from three male donor mice for each syngeneic transplant (42 mice in total). Forty age-matched male mice (inbred 129X1/SvJ mice, JAX stock #000691, The Jackson Laboratory, Bar Harbor, ME, USA) were divided into the following groups: Sham-operated (Sham group, n=4); left anterior descending artery (LAD) ligation to induce MI (MI group, n=9); LAD ligation followed by epicardial transplantation of ECM patch without AAMs (ECM patch group, n=13); and LAD ligation followed by AAMs patch, an ECM patch with AAMs, transplantation (AAMs patch group, n=14). Cardiac function was evaluated weekly by ECHO, and after an 8-week follow-up, animals were sacrificed and hearts collected for analyses, including: (1) ANP expression with qRT-PCR from heart apices, (2) ventricular morphometric assessment with wall thickness, scar transmurality and planimetric measurements, (4) histological evaluation for myocardial preservation with antibody and PicroSirius Red stain against cTnT and collagens, respectively. Collagen staining was further supplemented with microscopy using circularly polarized light to subtype mature (type I) and immature (type III) collagens.

Another set of mice was used to evaluate the mechanisms of AAMs. Male mice (strain 129X1/SvJ) were divided into three groups to receive either epicardial ECM (n=7) or AAMs (n=7) patch therapy after MI or Sham control (n=4). As previously described, animals were sacrificed, hearts were collected, but here cryopreserved after the 8-week follow-up. Transplant, subtransplant and remote septal tissue samples were dissected from thin cryosections and subsequently processed for label-free site-targeted proteomic analysis (DIA-nanoLC-HD-MS^{E}; AAMs patch, n=4x3; ECM patch, n=4x3). Prior to bioinformatic analyses using IPA® software, the proteomic data were scrutinized by Principal Component Analysis, resulting in the exclusion of outliers, and by Spearman correlation heatmap. The results were validated using antibody staining on tissues

(targeting POSTN, TGM2 and GPX1 proteins) and by qRT-PCR, assaying *Postn*, *Tgm2*, *Gpx3* and *Myh7* mRNA transcripts. The proteomics data have been deposited to the Mass Spectrometry Interactive Virtual Environment (MassIVE; dataset MSV000084120).

Author affiliations

X.Y. and Mi. L. planned and performed experimental research, performed and supervised analyses, and wrote the article; J.T. planned and carried out immunohistochemistry, histomorphometry, image analysis, and wrote the article; V.S., Ma.L. and R.S. planned and performed proteomics analyses and bioinformatics, immunohistochemistry and wrote the article; E.M., M.K., A.H. and Z.Z. planned studies, provided critical resources and funding; E.K. planned and supervised the study, performed analyses, provided critical resources and funding, and wrote the article; all authors contributed to the writing and editing of the manuscript.

Acknowledgments

The authors thank Päivi Leinikka for her invaluable help in carrying out the animal experiments, Lahja Eurajoki and Nada Bechara-Hirvonen for their expert laboratory assistance and MSc Sole Lätti for the illustrations. Tissue processing was carried out at the Tissue Preparation and Histochemistry Unit of the Faculty of Medicine, University of Helsinki. Scanning of histological sections on slides was carried out at the Digital Microscopy and Molecular Pathology Unit, Institute for Molecular Medicine Finland (FIMM). Proteomics analyses were performed at the Meilahti Clinical Proteomics Core Facility, HiLIFE supported by Biocenter Finland.

Sources of funding

Finnish Funding Agency for Technology and Innovation (3137/31/2013, E.K.), Finnish state research funding for expert responsibility area (TYH215311/M.K., TYH2012203/A.H.), Academy of Finland (275882/E.M.), and Finnish Foundation for Cardiovascular Research (2016/E.M.).

Disclosure of conflict of interest

None for the authors. Antonio Graziano, a manuscript nonauthor member of the AADC consortium, is the founder of and owns stock in HBW srl, manufacturer of the Rigenera HBW tissue processor.

Correspondence and requests for materials should be addressed to E.K.

References

1. Wang H, Naghavi M, Allen C, et al. Global, regional, and national life expectancy, all-cause mortality, and cause-specific mortality for 249 causes of death, 1980-2015: a systematic analysis for the Global Burden of Disease Study 2015. Lancet 2016;388(10053):1459-1544.
2. Thygesen K, Alpert JS, Jaffe AS, et al. Fourth Universal Definition of Myocardial Infarction (2018). Circulation 2018;138(20):e618-e651.
3. Braunwald E. Heart failure. JACC Heart Fail 2013;1(1):1-20.
4. Desta L, Jernberg T, Löfman I, et al. Incidence, temporal trends, and prognostic impact of heart failure complicating acute myocardial infarction. The SWEDEHEART Registry (Swedish Web-System for Enhancement and Development of Evidence-Based Care in Heart Disease Evaluated According to Recommended Therapies): a study of 199,851 patients admitted with index acute myocardial infarctions, 1996 to 2008. JACC Heart Fail 2015;3(3):234-242.
5. Lampinen M, Vento A, Laurikka J, et al. Rational Autologous Cell Sources For Therapy of Heart Failure - Vehicles and Targets For Gene and RNA Therapies. Curr Gene Ther 2016;16(1):21-33.
6. Hashimoto H, Olson EN, Bassel-Duby R. Therapeutic approaches for cardiac regeneration and repair. Nat Rev Cardiol 2018;15(10):585-600.
7. Fisher SA, Brunskill SJ, Doree C, Mathur A, Taggart DP, Martin-Rendon E. Stem cell therapy for chronic ischaemic heart disease and congestive heart failure. Cochrane Database Syst Rev 2014;(4):CD007888.
8. Messina E, De Angelis L, Frati G, et al. Isolation and expansion of adult cardiac stem cells from human and murine heart. Circ Res 2004;95(9):911-921.
9. Meilhac SM, Buckingham ME. The deployment of cell lineages that form the mammalian heart. Nat Rev Cardiol 2018;15(11):705-724.
10. Koninckx R, Daniëls A, Windmolders S, et al. The cardiac atrial appendage stem cell: a new and promising candidate for myocardial repair. Cardiovasc Res 2013;97(3):413-423.

11. Leinonen JV, Emanuelov AK, Platt Y, et al. Left atrial appendages from adult hearts contain a reservoir of diverse cardiac progenitor cells. PLoS One 2013;8(3):e59228.

12. Detert S, Stamm C, Beez C, et al. The atrial appendage as a suitable source to generate cardiac-derived adherent proliferating cells for regenerative cell-based therapies. J Tissue Eng Regen Med 2018;12(3):e1404-e1417.

13. Fanton Y, Houbrechts C, Willems L, et al. Cardiac atrial appendage stem cells promote angiogenesis in vitro and in vivo. J Mol Cell Cardiol 2016;97:235-244.

14. Lampinen M, Nummi A, Nieminen T, Harjula A, Kankuri E. Intraoperative processing and epicardial transplantation of autologous atrial tissue for cardiac repair. J Heart Lung Transplant 2017;36(9):1020-1022.

15. Nummi A, Nieminen T, Pätilä T, et al. Epicardial delivery of autologous atrial appendage micrografts during coronary artery bypass surgery-safety and feasibility study. Pilot Feasibility Stud 2017;3:74.

16. Frangogiannis NG. Matricellular proteins in cardiac adaptation and disease. Physiol Rev 2012;92(2):635-688.

17. Zhang B, Wang J, Wang X, et al. Proteogenomic characterization of human colon and rectal cancer. Nature 2014;513(7518):382-387.

18. Trovato L, Monti M, Del Fante C, et al. A New Medical Device Rigeneracons Allows to Obtain Viable Micro-Grafts From Mechanical Disaggregation of Human Tissues. J Cell Physiol 2015;230(10):2299-2303.

19. Lalowski MM, Björk S, Finckenberg P, et al. Characterizing the Key Metabolic Pathways of the Neonatal Mouse Heart Using a Quantitative Combinatorial Omics Approach. Front Physiol 2018;9:365.

20. Nakada Y, Canseco DC, Thet S, et al. Hypoxia induces heart regeneration in adult mice. Nature 2017;541(7636):222-227.

21. Kimura W, Xiao F, Canseco DC, et al. Hypoxia fate mapping identifies cycling cardiomyocytes in the adult heart. Nature 2015;523(7559):226-230.

22. Kimura W, Sadek HA. The cardiac hypoxic niche: emerging role of hypoxic microenvironment in cardiac progenitors. Cardiovasc Diagn Ther 2012;2(4):278-289.

23. Puente BN, Kimura W, Muralidhar SA, et al. The oxygen-rich postnatal environment induces cardiomyocyte cell-cycle arrest through DNA damage response. Cell 2014;157(3):565-579.

24. Kühn B, del Monte F, Hajjar RJ, et al. Periostin induces proliferation of differentiated cardiomyocytes and promotes cardiac repair. Nat Med 2007;13(8):962-969.

25. Chen Z, Xie J, Hao H, et al. Ablation of periostin inhibits post-infarction myocardial regeneration in neonatal mice mediated by the phosphatidylinositol 3 kinase/glycogen synthase kinase 3β/cyclin D1 signalling pathway. Cardiovasc Res 2017;113(6):620-632.

26. Mirotsou M, Jayawardena TM, Schmeckpeper J, Gnecchi M, Dzau VJ. Paracrine mechanisms of stem cell reparative and regenerative actions in the heart. J Mol Cell Cardiol 2011;50(2):280-289.

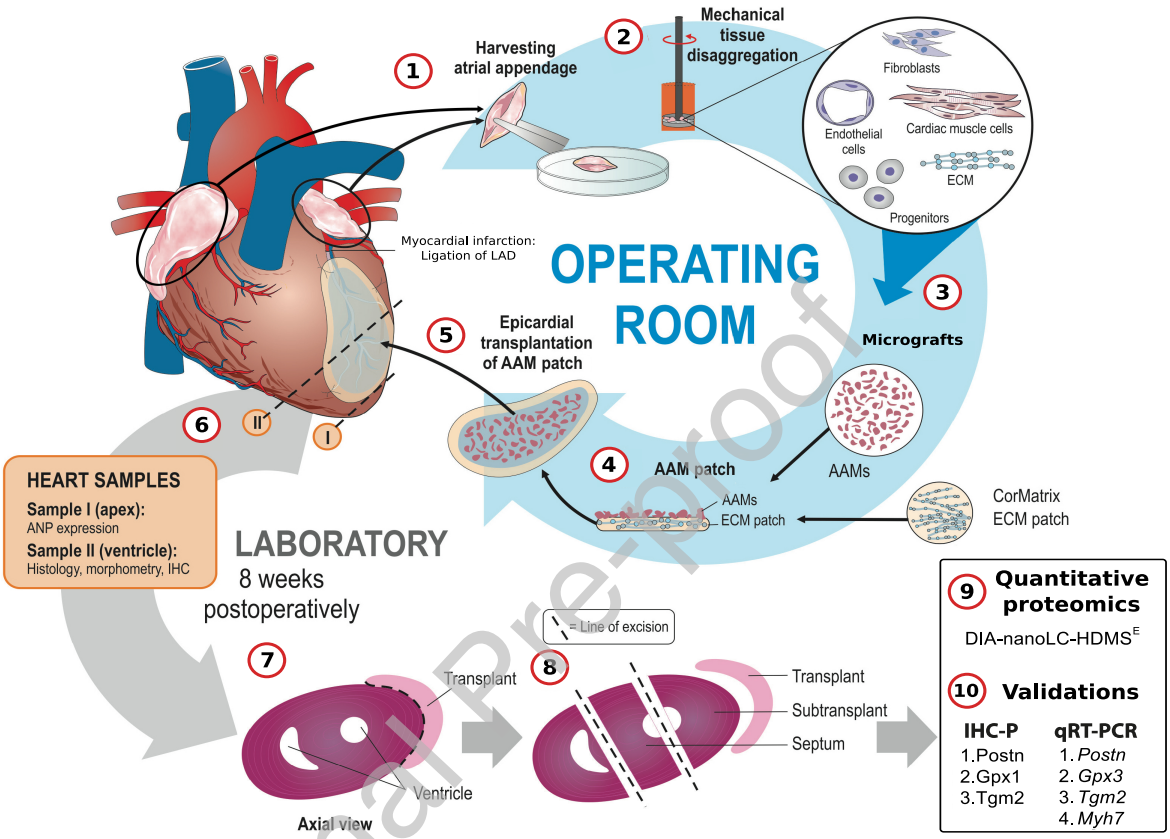

Figure 1. Overview of the study protocol.
A schematic presentation of the processes carried out in the operating room and subsequently in the laboratory are illustrated. For further information, see the Detailed Materials and Methods. **1.** For each AAMs patch, both left and right atrial appendages were harvested from three syngeneic donor mice after placement of an atrial clip. **2.** and **3.** Harvested appendages were disaggregated to atrial appendage micrografts (AAMs) with a Rigenera machine. **4.** An ECM sheet (CorMatrix® ECM™ for cardiac tissue repair) was peeled into four layers, and 1-ply sheets were cut into circles using an 8 mm diameter tissue punch. To create an AAMs patch, we evenly dispersed the AAMs suspension, containing tissue material from six appendages (three from both the right and left sides), onto the matrix sheet and sealed with a thin layer (10 µl volume) of fibrin tissue glue. **5.** The AAMs patch was subsequently fitted onto the recipient heart with the AAMs-containing side facing the epicardium of the left ventricle at the site of infarction. The transplant was further fixed to the myocardium by three sutures to ensure that the patches remained in place. **6.** After the 8-week follow-up, animals were sacrificed, hearts were excised, and ventricular tissue samples were collected for histology or snap frozen in liquid nitrogen. Apices were also collected for the measurement of ANP mRNA expression with qRT-PCR. **7.** Thin histological sections were used for immunohistochemistry and morphometry. **8.** and **9.** Cryosections of 12-µm thickness were collected from three anatomic groups (transplant/patch, subtransplant and septum) for proteomic profiling. **10.** Lastly, rest of the cryopreserved samples were used for selected validative qRT-PCR measurements, and paraffin embedded tissue samples for IHC-P staining.

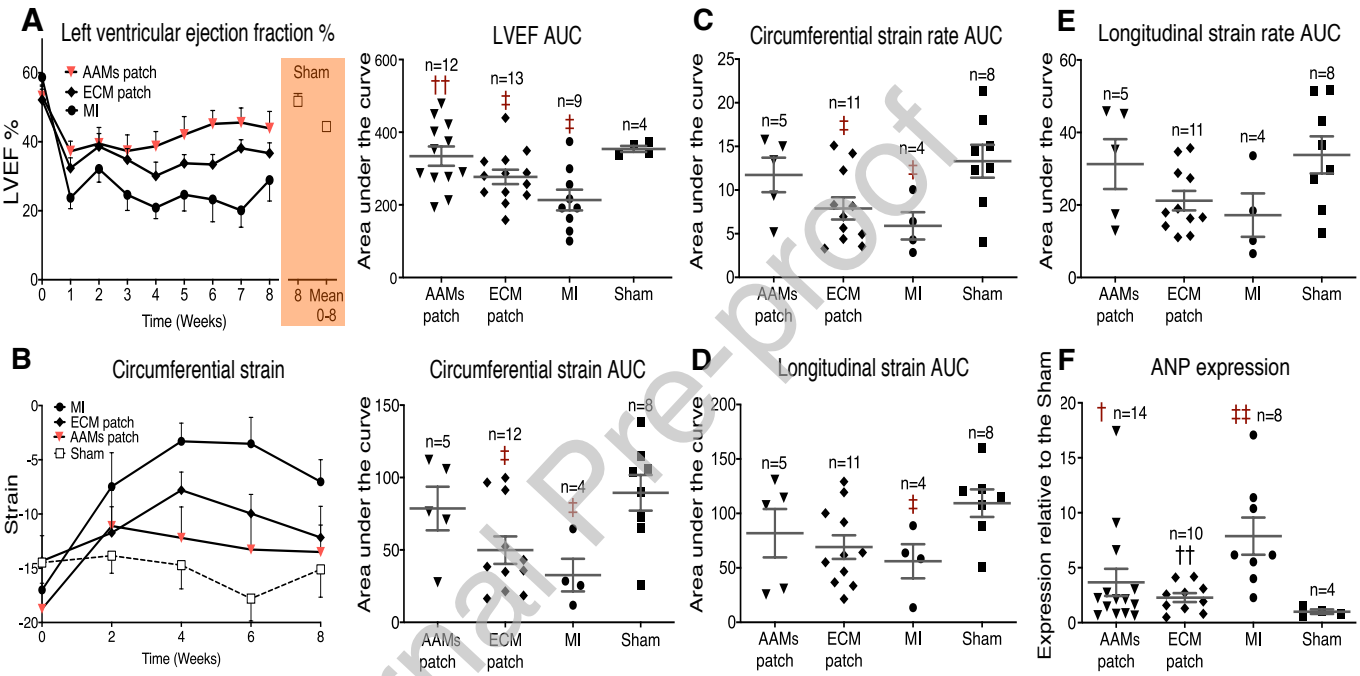

Figure 2. Myocardial function.

A, left panel shows weekly performed LVEF measurements; right panel shows AUC analysis from the LVEF follow-up data. **B**, left panel shows the circumferential strain measured with ECHO at 2-week intervals; the right panel shows the corresponding AUC. **C**, AUC analysis of the circumferential strain rate. **D**, AUC analysis of the longitudinal strain; **E**, AUC analysis of the longitudinal strain rate. **F**, relative expression of ANP mRNA to expression of 18S mRNA from apex tissue samples as analyzed by real-time PCR. */†/‡, *p*-value <0.05; **/††/‡‡, *p*-value <0.01; ***/†††/‡‡‡, *p*-value <0.001; *, *p*-value vs. the ECM patch group; †, *p*-value vs. the MI group; ‡, *p*-value vs. the Sham group. Two-tailed Mann-Whitney *t*-test was applied and data normality assessed with Shapiro-Wilk test for normality. The scatter plot data represent mean ± SEM. The n-values represent separate mice measured with high confidence and in regard to ANP expression, number of analyzed heart apices.

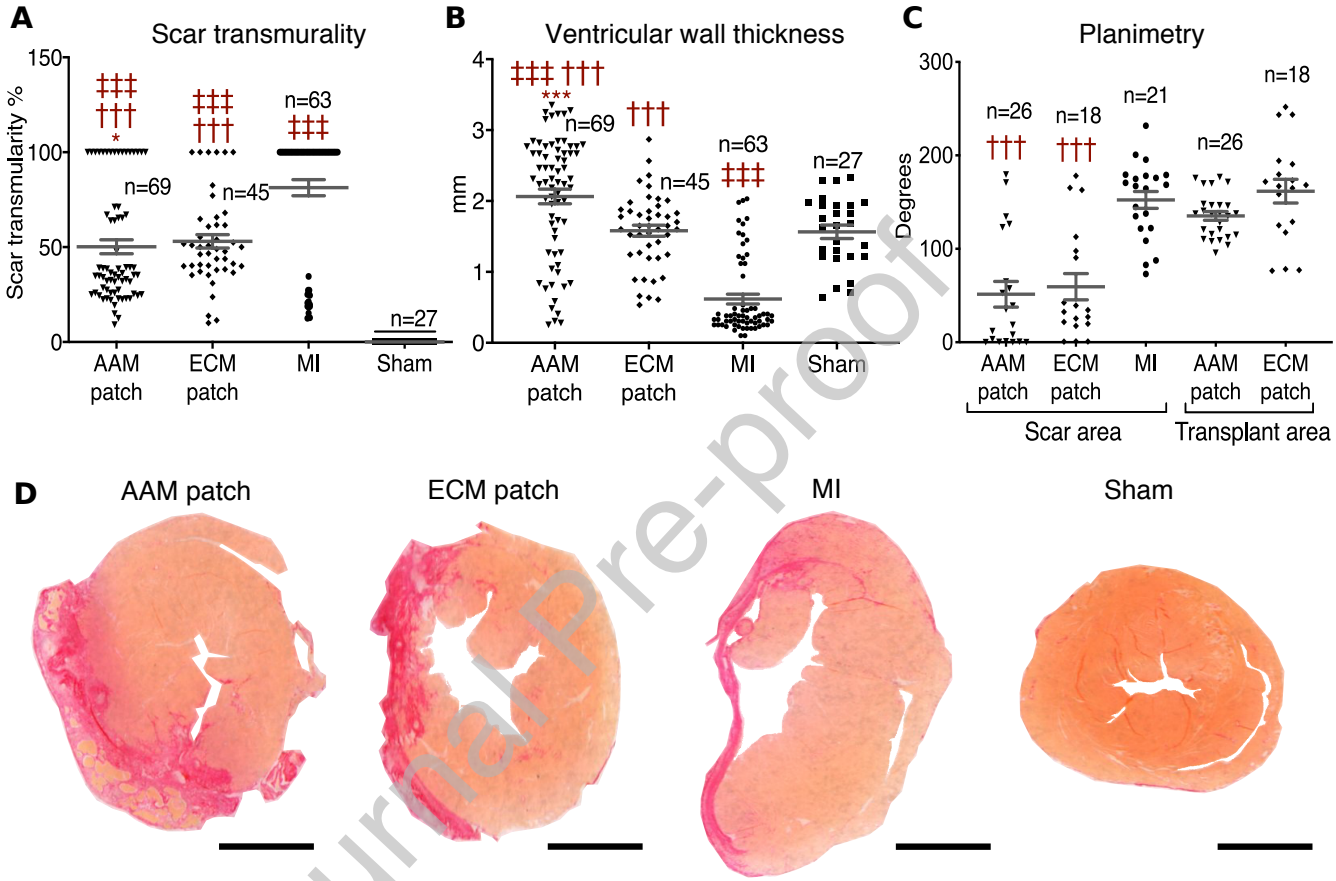

Figure 3. Ventricular morphometry.

A, infarction scar transmurality assessed by measuring the thickness of collagen-containing tissue and comparing it to the total thickness of the ventricular wall. **B**, ventricular wall thickness; thickness of the transplant was included in the measurement. **C**, planimetry analysis of the infarction scar angle. **D**, representative sections of Picrosirius Red-stained tissue samples assessed for tissue morphometry and infarction scar transmurality. Scale bars equal 2mm. */†/‡, *p*-value <0.05; **/††/‡‡, *p*-value <0.01; ***/†††/‡‡‡, *p*-value <0.001; *, *p*-value vs. the ECM patch group; †, *p*-value vs. the MI group; ‡, *p*-value vs. the Sham group. Two-tailed Mann-Whitney *t*-test was applied and data normality assessed with Shapiro-Wilk test for normality. From each heart sample, three adjacent histological sections were cut for analysis. The n-values represent total measurement sites assessed with high confidence (**A** and **B**, 9 measurements/sample; **C** 3 measurements/ sample).

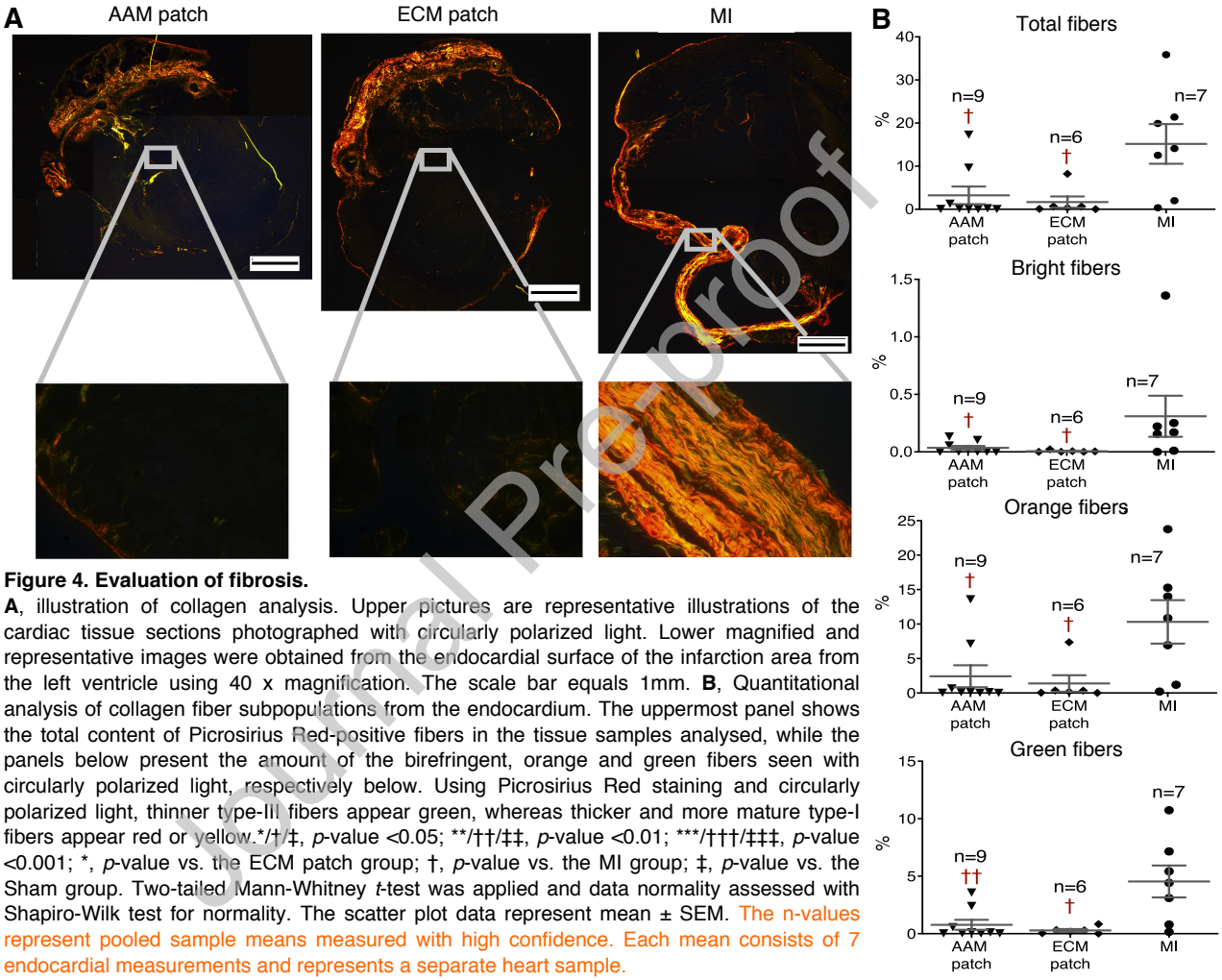

Figure 4. Evaluation of fibrosis.

A, illustration of collagen analysis. Upper pictures are representative illustrations of the cardiac tissue sections photographed with circularly polarized light. Lower magnified and representative images were obtained from the endocardial surface of the infarction area from the left ventricle using 40 x magnification. The scale bar equals 1mm. **B**, Quantitational analysis of collagen fiber subpopulations from the endocardium. The uppermost panel shows the total content of Picrosirius Red-positive fibers in the tissue samples analysed, while the panels below present the amount of the birefringent, orange and green fibers seen with circularly polarized light, respectively below. Using Picrosirius Red staining and circularly polarized light, thinner type-III fibers appear green, whereas thicker and more mature type-I fibers appear red or yellow.*/†/‡, *p*-value <0.05; **/††/‡‡, *p*-value <0.01; ***/†††/‡‡‡, *p*-value <0.001; *, *p*-value vs. the ECM patch group; †, *p*-value vs. the MI group; ‡, *p*-value vs. the Sham group. Two-tailed Mann-Whitney *t*-test was applied and data normality assessed with Shapiro-Wilk test for normality. The scatter plot data represent mean ± SEM. The n-values represent pooled sample means measured with high confidence. Each mean consists of 7 endocardial measurements and represents a separate heart sample.

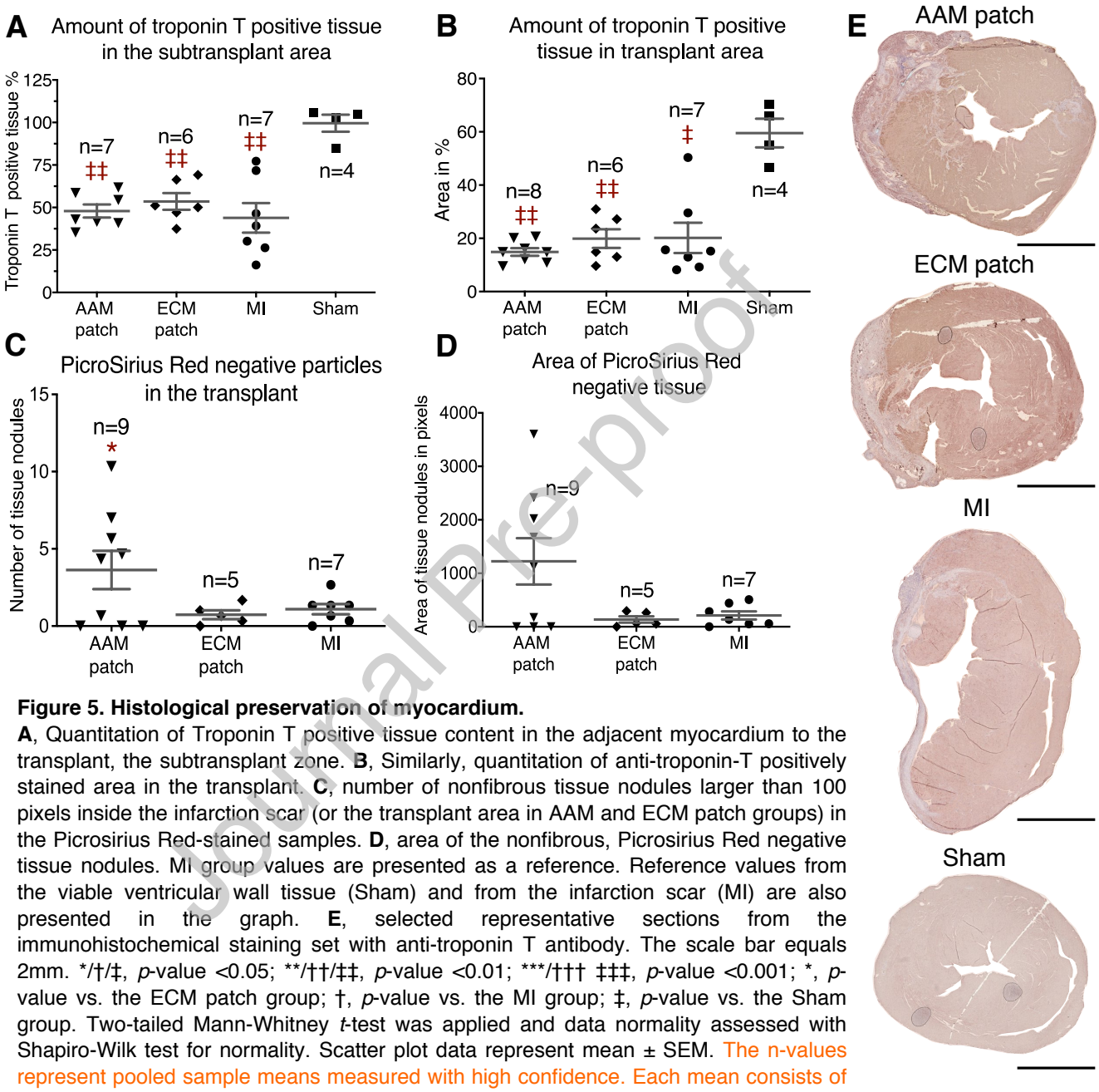

Figure 5. Histological preservation of myocardium.
A, Quantitation of Troponin T positive tissue content in the adjacent myocardium to the transplant, the subtransplant zone. **B**, Similarly, quantitation of anti-troponin-T positively stained area in the transplant. **C**, number of nonfibrous tissue nodules larger than 100 pixels inside the infarction scar (or the transplant area in AAM and ECM patch groups) in the Picrosirius Red-stained samples. **D**, area of the nonfibrous, Picrosirius Red negative tissue nodules. MI group values are presented as a reference. Reference values from the viable ventricular wall tissue (Sham) and from the infarction scar (MI) are also presented in the graph. **E**, selected representative sections from the immunohistochemical staining set with anti-troponin T antibody. The scale bar equals 2mm. */†/‡, *p*-value <0.05; **/††/‡‡, *p*-value <0.01; ***/††† ‡‡‡, *p*-value <0.001; *, *p*-value vs. the ECM patch group; †, *p*-value vs. the MI group; ‡, *p*-value vs. the Sham group. Two-tailed Mann-Whitney *t*-test was applied and data normality assessed with Shapiro-Wilk test for normality. Scatter plot data represent mean ± SEM. The n-values represent pooled sample means measured with high confidence. Each mean consists of multiple measurements and represents a separate heart sample.

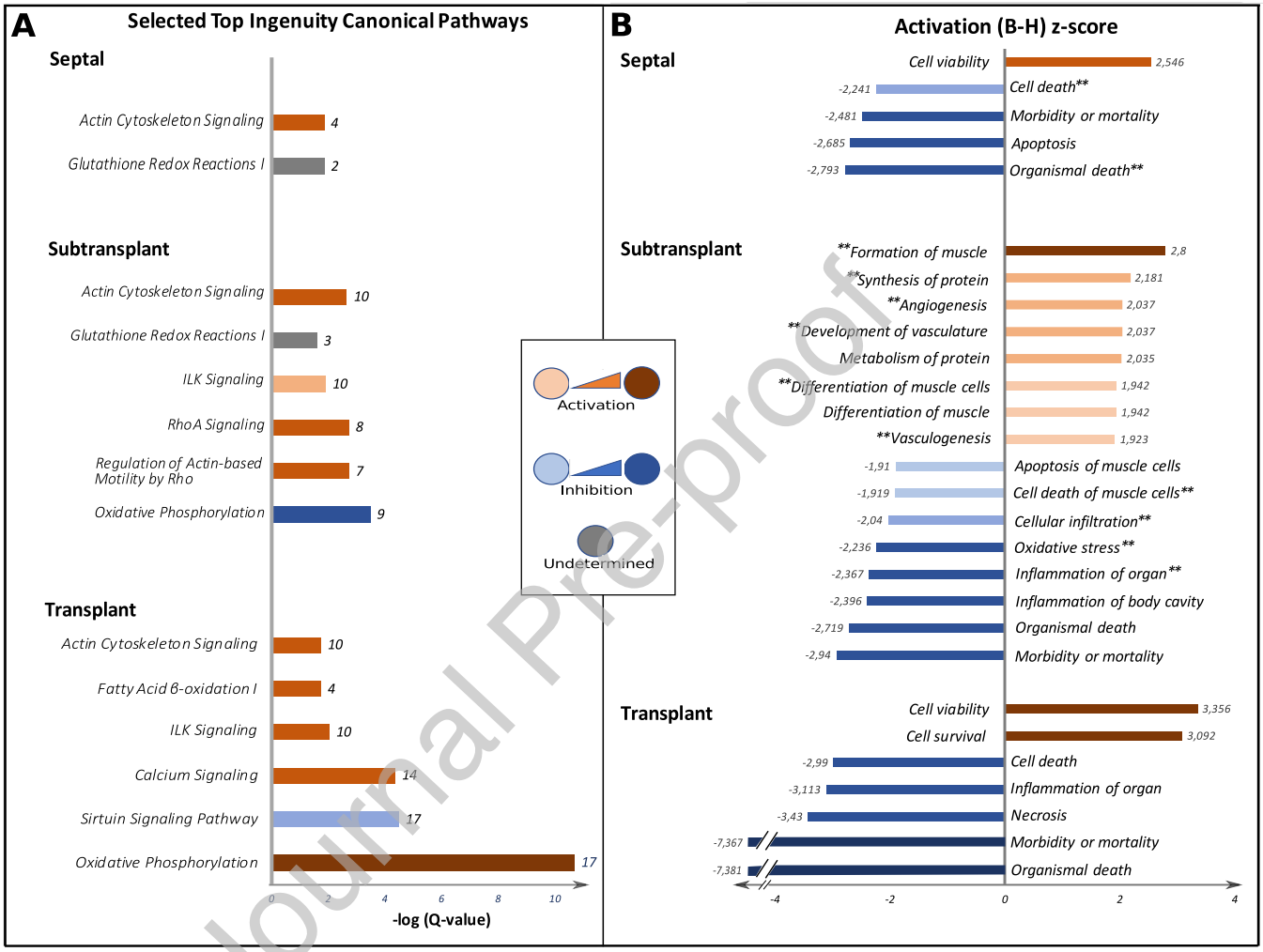

Figure 6. Proteomics, canonical pathways and biological functions.
From each anatomical site, selected canonical pathways (**A**) and functions (**B**) are shown. The results are based on IPA® software analysis of given representative locational DEPs (shown in Data File S1). The Q-value represents the B-H *p*-value (Benjamini-Hochberg corrected *p*-value). Q-value ≥ 1.5 and |z-score| ≥ 2 were used as criteria for significant activation or inactivation of a given pathway or process. All detected changes were compared to the ECM patch group, thus, these changes were attributed to AAMs transplantation. At the end of each bar in the subplot (**A**) is the number of DEPs associated with a given pathway while in (**B**) the approximate z-score values are presented. Functions annotated with double asterisk (**) are shown further in Figure 7. All canonical pathways as well as diseases and functions identified in each anatomical site are provided in Figures S3 and S4, respectively.

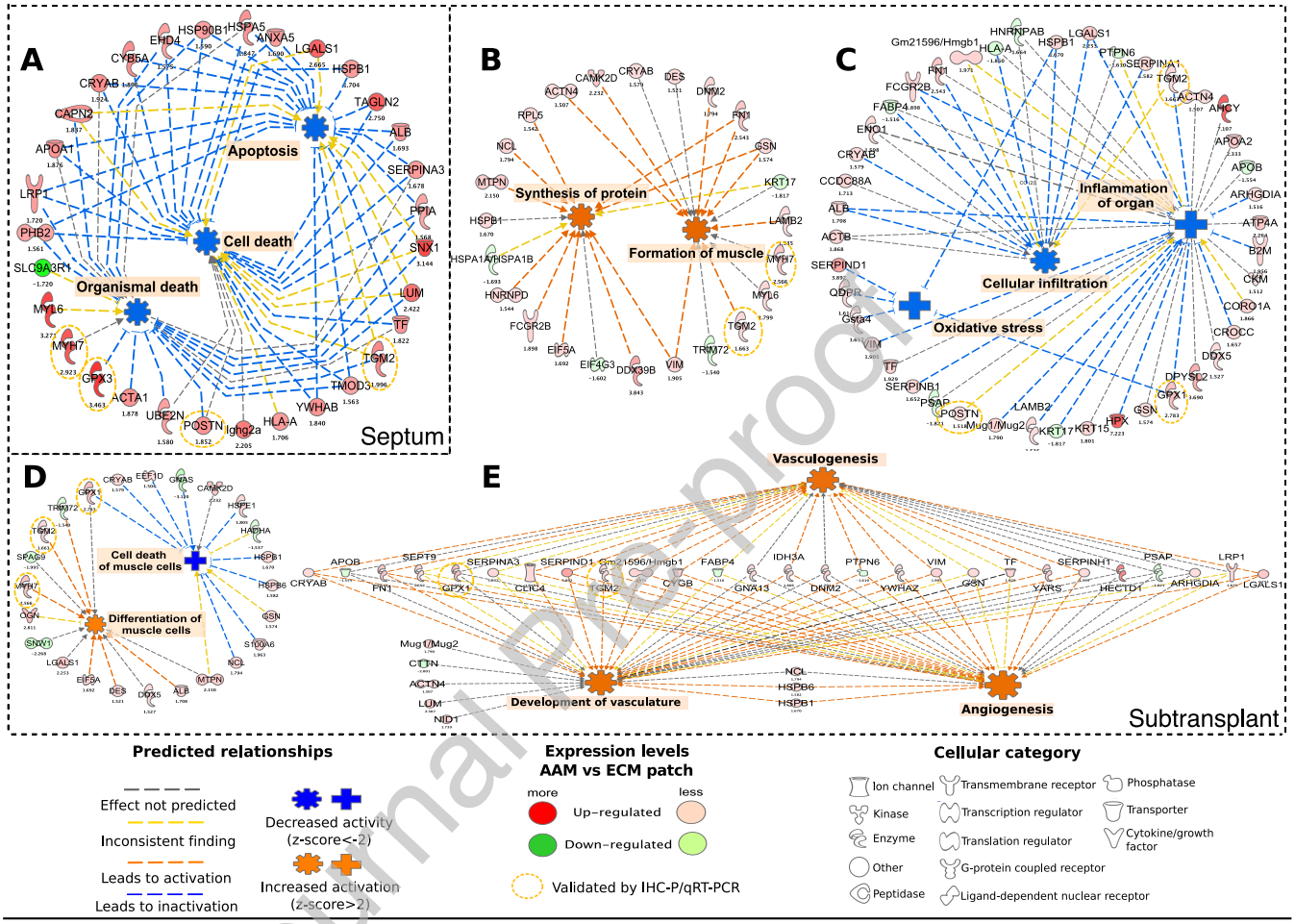

Figure 7. DEPs and associated biological functions.
Selected biological functions from Figure 6 and associated DEPs are shown here. **A**, prosurvival functions and associated DEPs from the remote septum are presented. Periostin (POSTN) is documented cardiomyocyte mitogen and repair-mediator after ischemic cardiac damage. **B**, functions related to anabolic protein and muscle metabolism from the subtransplant are shown. Desmin (DES) is a pivotal intermediate filament in cardiomyocytes while Myosin 7 (MYH7) is a major slow twitch myosin isoform in the heart. **C**, DEPs associated with a decreased inflammatory reaction in the subtransplant are shown. Glutathione Peroxidase 1 (GPX1) is a ubiquitous enzyme with antioxidant properties catalysing the hydrolysis of hydrogen peroxide radical to water. **D**, DEPs associated with increased cardiomyocyte differentiation in the subtransplant immediately next to AAMs patch transplantation are shown. However, these functions showed only substantially strong trends towards activation and inactivation with a |z-score| = 1.9 for both functions (with criterion for significant activation or inactivation being |z-score| ≥ 2.0). **E**, functions related to angiogenesis with associated DEPs in the subtransplant are shown. Transglutaminase 2 (TGM2) catalyses crosslinking of proteins and is associated in apoptosis, it is also documented to be prosurvival factor for cardiomyocytes following ischemic insult. Small numeric counts below each DEP represent the expression ratio in AAMs patch group divided by that of the ECM patch group. Statistical significance for differential protein expression was assessed using two-way ANOVA with *p*-value criterion ≤ 0.05.

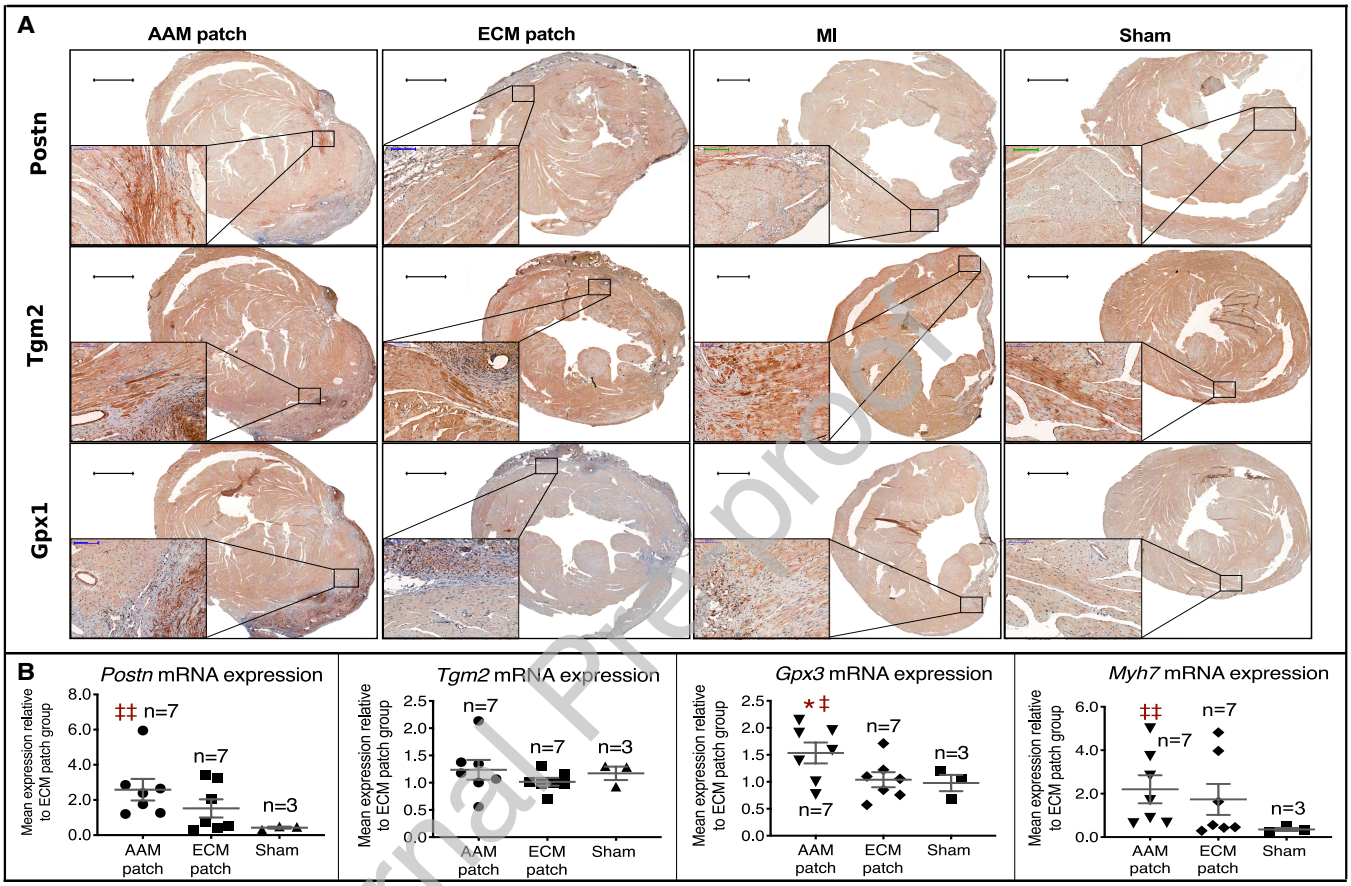

Figure 8. Validative IHC-P and qRT-PCR analyses.

The set of samples preserved in paraffin was used for evaluating the fibrotic content and overall histomorphology of the study groups by IHC-P. Assessment by qRT-PCR was applied for the same set of cryopreserved samples as in the quantitative proteomics. **A**, The representative images with magnifying subcaptions from the IHC-P stainings are presented here for three selected proteins of interest: POSTN, TGM2 and GPX1 (n=4 for each). POSTN exhibited marked expression in the patch zone as well as in the extracellular interphase of fibrotic scar areas and myocardium in all groups. TGM2 expression was mainly localized to the intracellular compartment of cardiomyocytes and endothelial cells, with the most pronounced expression localizing to the cardiomyocytes with immediate contact to the fibrotic areas in the subtransplant zone right below the patch. Finally, the GPX1 exhibited marked expression in the patch itself and in the vascular wall. Intracellular expression in cardiomyocytes seemed to be more pronounced in AAMs group as compared to the ECM group. The black, green and blue scale bars equal 1000µm, 200µm and 100µm, respectively. **B**, The results of the qRT-PCR. Transcription of *Myh7*, *Gpx3* and *Postn*, together with the production of the corresponding mRNAs, was significantly higher after AAMs patch transplantation (n=7) in comparison to the ECM patch transplantation (n=7), when both were compared against the steady state gene expression represented by the Sham expression levels (n=3). *Tgm2* expression was not altered. */ ‡, *p*-value <0.05; **/‡‡, *p*-value <0.01; *, *p*-value vs. the ECM patch group; ‡, *p*-value vs. the Sham group. The *p*-values were calculated using one-way unpaired *t*-test with Welch's correction for unequal variances. Normality of the data was assessed with Shapiro-Wilk normality test. The scatter plot data represents mean ± SEM. The n-values represent separate heart cryosamples measured with high confidence (1 cryosample/individual).